Inferred pyrite growth via the particle attachment pathway in the presence of trace metals
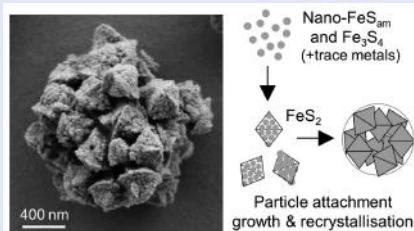
J.M. Domingos[1], E. Runge[1], C. Dreher[2], T.-H. Chiu[2], J. Shuster[3], S. Fischer[3], A. Kappler[2,4], J.-P. Duda[1], J. Xu[5,6], M. Mansor[2,5*]

OPEN ACCESS

Abstract

The morphology of pyrite has been used to infer ancient redox states and biogenicity. However, the influence of trace metals on pyrite morphology is poorly understood. Through batch synthesis experiments, we demonstrate that bioessential trace metals (Co, Cu, Mo, Ni, Zn) accelerate pyrite formation. The first precipitate, FeS_{am}, transformed to an intermediate greigite phase and to pyrite with increasing time and temperature. Trace metals either facilitated polysulphide formation or precipitated as nanoparticles that can serve as nuclei for pyrite growth, depending on the initial metal concentration. Despite varying precipitation rates, the final pyrite morphologies were unaffected. Various morphologies including tabular precipitates (<150 nm), aggregates resembling microframboids (100–250 nm), octahedral (300–1500 nm) and rose-like particles (1000–3000 nm) were observed. This size–shape particle continuum was interpreted as stages of pyrite growth via particle attachment. This process could be important in explaining variations in the mineral's reactivity (e.g., defects), isotopic and trace metal distributions, and morphologies (e.g., framboids) for applications in paleo-proxies, environmental research and biosignatures.

Introduction

Pyrite is a widespread mineral that is involved in a variety of biogeochemical processes with implications for interpreting Earth's past, present and future (Huang et al., 2017). Natural pyrite typically adopts either a euhedral or framboidal (raspberry-like) morphology. Euhedral pyrite is proposed to form via slow growth on pre-existing pyrite, while framboids are proposed to form under fast nucleation conditions in close association with Fe sulphide precursors, such as mackinawite (FeS) and greigite (Fe_3S_4) (Raiswell, 1982; Butler and Rickard, 2000). In the geological record, high abundances of framboids have been interpreted as indicators of euxinic conditions in water columns (Wilkin et al., 1996; Rickard, 2019). The striking morphology of framboids and their association with organic matter have led to their interpretation as biosignatures, despite the various reports of framboid synthesis via abiotic pathways (Ohfuji and Rickard, 2005).

The continuum model for pyrite growth (Sawlowicz, 1993) has received increasing support from growing textural, geochemical and isotopic evidence (Lin et al., 2016, 2017; Liu et al., 2022). In this model, pyrite of different morphologies and sizes reflects cyclic growth stages of small euhedral particles aggregating to form framboids that recrystallise over time into a larger euhedral particle. This continuum model mirrors the particle attachment pathway in that mineral growth occurs via aggregation and recrystallisation of smaller particles. This pathway explains defects in crystal structures, distributions of trace metals and isotopes, and unusual particle morphologies in nature (De Yoreo et al., 2015). This pathway has been demonstrated for pyrite synthesised at >100 °C (Hunger and Benning, 2007; Li et al., 2011; Gong et al., 2013), but not at lower temperatures.

Recent studies have investigated how trace metals impact pyrite formation rates (Table S-1). Comparatively, the effects of trace metals on pyrite morphology are under-constrained. Here, we tested the influence of five bioessential trace metals (Co, Cu, Mo, Ni, Zn) on pyrite formation. These bioessential trace metals are common impurities in pyrite and play key roles in Earth's biogeochemical evolution (Robbins et al., 2016). Their effects on pyrite formation need to be constrained in order to disentangle factors that can affect the utility of pyrite morphologies as environmental proxies and biosignatures.

Fe Sulphide Transformation Sequence

Iron sulphides were synthesised in the presence of 3 mM Fe^{2+}, 6 mM Na_2S and 30 mM elemental sulphur (S^0) in 50 mM HEPES buffer (pH 7). Two sets of experiments were performed and

termed *Set-1* (97 % N_2, 3 % H_2 headspace) and *Set-2* (100 % N_2), respectively (details in SI Methods; Table S-2). In both sets, the addition of Na_2S to Fe^{2+} led to the immediate formation of fine black precipitates identified as a disordered mackinawite-like phase (FeS_{am}) based on a single broad reflection with d-spacings of 5.2–5.3 Å via X-ray diffraction (XRD) (Fig. 1a; Table S-3), and characteristic sheet-like aggregate structures under scanning electron microscopy (SEM) (Fig. 2a) (Csákberényi-Malasics *et al.*, 2012).

Despite following the same methods, *Set-1* and *Set-2* experiments demonstrated differences in greigite contents, pyrite formation rates and the extent of pyritisation. In *Set-1* experiments, FeS_{am} transformed to greigite and eventually to pyrite with increasing time (up to 14 days) and temperature (25–80 °C). FeS_{am} was no longer detectable by XRD after 14 days of incubation at 80 °C, but greigite was still not fully transformed to pyrite (Fig. 1a). Comparatively, in *Set-2* experiments, FeS_{am} was completely transformed to pyrite within 3–7 days of incubation at 80 °C, with no greigite detected. Nonetheless, greigite was likely present at low relative abundances because minerals attracted to hand magnets were observed (Table S-3). These magnetic minerals were associated with black coatings around S^0 particles.

Samples containing greigite and pyrite from *Set-1* experiments were analysed using SEM, which revealed morphologies classified into four categories: tabular (<150 nm), spherical aggregates (100–250 nm), octahedral (300–1500 nm) and rose-like particles (1000–3000 nm) (Fig. 2). Treatment with 6 M HCl led to dissolution of the tabular particles, which we interpret as HCl-soluble greigite given its morphological similarity to previous lab-synthesised greigite (Csákberényi-Malasics *et al.*, 2012; Mansor *et al.*, 2019). The other particles (spherical aggregates, octahedra and "roses") were interpreted as pyrite since they did not dissolve in HCl (Voelz *et al.*, 2019). In *Set-2* experiments, where greigite was not detected by XRD, tabular particles were rarely observed whilst other particles were common. Occasionally, acicular particles (100–5000 nm length) were also observed from day 3 onwards and identified via energy dispersive X-ray spectroscopy (EDS) to be rich in Fe and oxygen, suggestive of Fe(III) oxyhydroxides (Fig. S-1).

Overall, *Set-1* and *Set-2* experiments exhibited similar transformation sequences of FeS_{am} to greigite to pyrite with increasing time and temperature, consistent with previous studies (Hunger and Benning, 2007; Mansor and Fantle, 2019). Alternative pathways without a greigite intermediate are possible (see Sanden *et al.*, 2021) but seem unlikely in our experiments. We suggest that the differences in pyrite formation rates (~10× faster in *Set-1*) are caused by the headspace composition (3 % H_2 vs. pure N_2). The lack of H_2 in *Set-2* experiments likely led to a more oxidising condition, which accelerated pyrite formation, consistent with the detection of trace Fe(III) oxyhydroxides (SI Discussion). Differences in headspace gas composition should be considered for experimental studies on pyrite.

Influence of Trace Metals on Pyrite Formation

Prior to Na_2S addition, trace metals (Co, Cu, Mo, Ni, Zn) were added to *Set-1* and *Set-2* experiments to obtain metal:Fe ratios of $1{:}10^5$ and $1{:}10^2$, respectively, to determine their effects on pyrite formation. These ratios represent the broad range of environments (e.g., low temperature sediments, acid mine drainage, hydrothermal vents) in which natural pyrite can form (Von Damm *et al.*, 1985; Shaw *et al.*, 1990; Allman *et al.*, 2021).

From the *low-metal* setups ($1{:}10^5$ ratio), XRD analysis suggested that all trace metals accelerated pyrite formation after 14 days of incubation at 80 °C. The ratio of pyrite/greigite increased in the following order: *no-metal* < Mo < Ni < Cu < Zn < Co, although it must be noted that the ratios overlap within error (Fig. 1b). We were unable to determine if any accelerating effects occurred in the *high-metal setups* ($1{:}10^2$) given the unexpectedly rapid pyrite formation within *Set-2* experiments. In both experimental sets, stronger magnetism was observed in the presence of Mo compared to other metals.

Trace metals were proposed to influence pyrite formation via either: (1) formation of metal-rich nanoparticles that serve as nuclei, (2) complexation or redox reactions that affect polysulphides reactivity and formation, and S(-II) and Fe(II) oxidation,
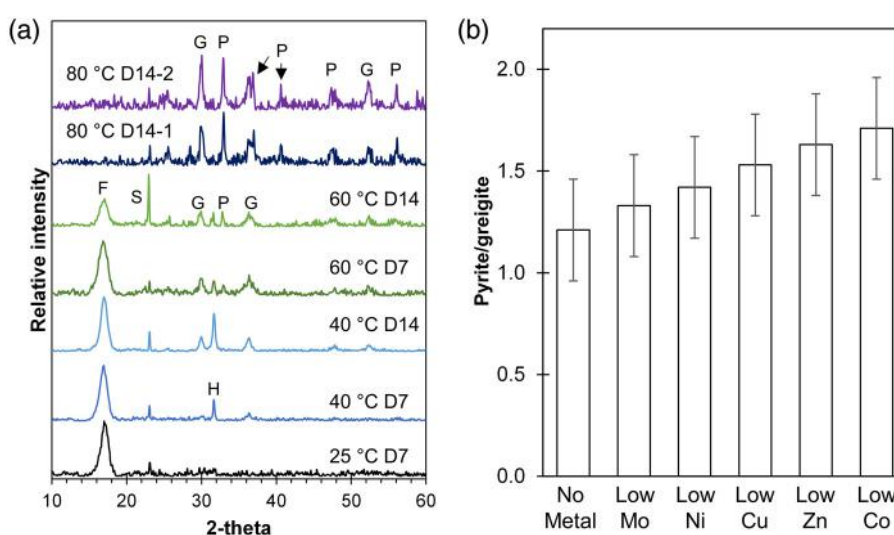
Figure 1 **(a)** XRD patterns showing the progressive transformation from FeS_{am} (F) to greigite (G) and pyrite (P) with increasing temperatures (25, 40, 60 and 80 °C) and time (after 7 and 14 days). Residual sulphur (S) and halite (H) were also detected. Samples from two replicate bottles of experiments at 80 °C after 14 days (80 °C D14-1 or D14-2) indicate high reproducibility. **(b)** Relative intensity of pyrite/greigite signals as determined from thin-film XRD after 14 days of incubation at 80 °C.
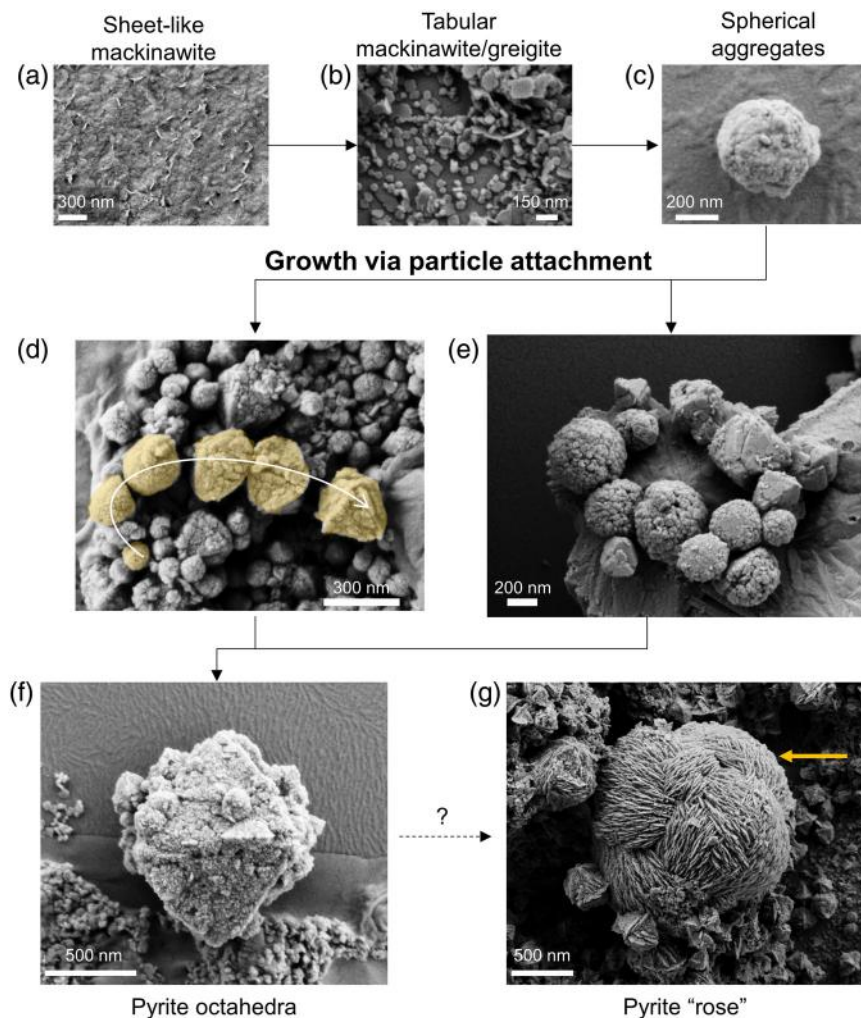
Figure 2 Representative SEM micrographs suggestive of growth via particle attachment. **(a–c)** Transformation of mackinawite to tabular greigite to spherical aggregates of tabular particles. **(d)** The arrow denotes a potential transformation from spherical aggregates to pyrite octahedra. **(e)** Close association between spherical aggregates (microframboids) that are recrystallising to form pyrite octahedra. **(f)** Colloidal pyrite octahedra (centre) with a rough surface and porous structure. **(g)** Micrometre-sized pyrite "rose" (yellow arrow) surrounded by smaller pyrite octahedra. The transformation mechanism may be related to skeletal growth.

or (3) stabilisation of FeS precursors via coprecipitation or adsorption (Table S-1). To test the first two possibilities, we repeated the *no-metal*, *low-metal* (30 nM metals) and *high-metal* (30 μM) setups with the omission of Fe and monitored the formation of nanoparticles and polysulphides at 80 °C.

In the *no-metal* and *low-metal* setups, no precipitates formed and a slight yellow tinge indicative of polysulphides was observed (Fig. 3a). The polysulphide spectra obtained by UV-VIS spectroscopy generally increased in intensity with time with two peaks observed at 275 and 314 nm. At day 1, higher polysulphide peaks were observed in the presence of Co, Cu, Ni and Zn relative to the *no-metal* setup (Fig. 3c–d; S-2). After day 8, however, polysulphides were elevated only in the presence of Co, while the other metals showed no increase or even a slight decrease compared to the *no-metal* setup. High polysulphides with Co correlated with increased pyrite formation rate (Fig. 1b), suggesting that the interaction between this metal and polysulphides may play a role in accelerating pyrite formation.

In the *high-metal* setups, grey or colourless precipitates were formed with all trace metals except for Mo. The yellow polysulphide tinge was evident in the presence of Mo, Cu and Zn

but was obscured by the presence of colloidal nanoparticles in the presence of Ni and Co (Fig. 3b). Polysulphide intensities increased with higher trace metal concentrations with the exception of Mo. High Mo concentration induced an additional peak at 470 nm corresponding to tetrathiomolybdate (MoS_4^{2-}) (Erickson and Helz, 2000). The highest polysulphide intensities at day 14 were observed in the presence of high Co concentration, followed by Ni, Cu and Zn (Fig. 3c–d). The amount of polysulphide formed was likely influenced by varying availability of H_2S and S^0 after metal sulphide precipitation. All the metals tested in this study were proposed to form polysulphide complexes (Rickard and Luther, 2006), with Co known to enhance polysulphide conversions in lithium-sulphur batteries (Liu *et al.*, 2021). The interactions between these metals and polysulphides and their impact on biogeochemistry are currently poorly known.

The tentative accelerating effects of Mo and Ni on pyrite formation observed in this study are consistent with previous studies (Table S-1). Mo is also known to promote greigite formation (Mansor and Fantle, 2019; Miller *et al.*, 2020), which could explain the lower pyrite/greigite ratio observed in the presence of Mo compared to other trace metals. In contrast, other studies demonstrated that Co and Ni (Swanner *et al.*, 2019) and Mo
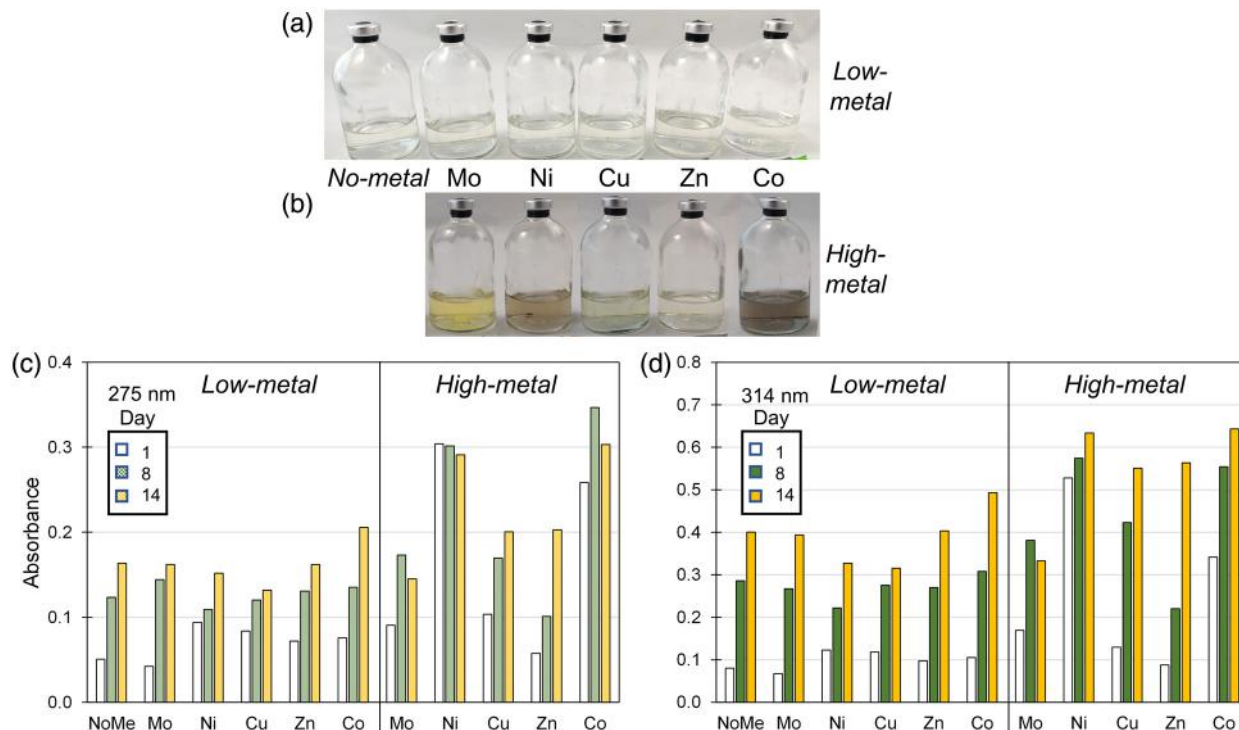
Figure 3 **(a–b)** Pictures of Fe-free setups after 8 days of incubation at 80 °C. Yellow tinge indicates the presence of polysulphides. Precipitates (grey or colourless) are observed in some *high-metal* setups. **(c–d)** Bar charts of the polysulphide peak intensities at (c) 275 nm and (d) 314 nm at Day 1, 8 and 14. Polysulphide intensities increase with time and with higher metal concentrations.

(Baya *et al.*, 2022) inhibited pyrite formation. Differences in metal:Fe ratios and synthesis conditions (*e.g.*, pH and formation pathways) between studies likely led to differences in how specific trace metals affect pyrite formation (SI Discussion). Nevertheless, our results clearly show that trace metals influence polysulphide chemistry and form metal-rich nuclei that may affect pyrite formation.

Despite differences in precipitation rates, the presence of trace metals had little influence on pyrite morphologies (Fig. S-3). Spherical aggregates, octahedral and rose-like particles interpreted as pyrite were present in all samples with no systematic correlation with precipitation rate. Therefore, we conclude that pyrite morphologies were unaffected by trace metal loading. Other factors, such as aging time, S/Fe ratio, organic

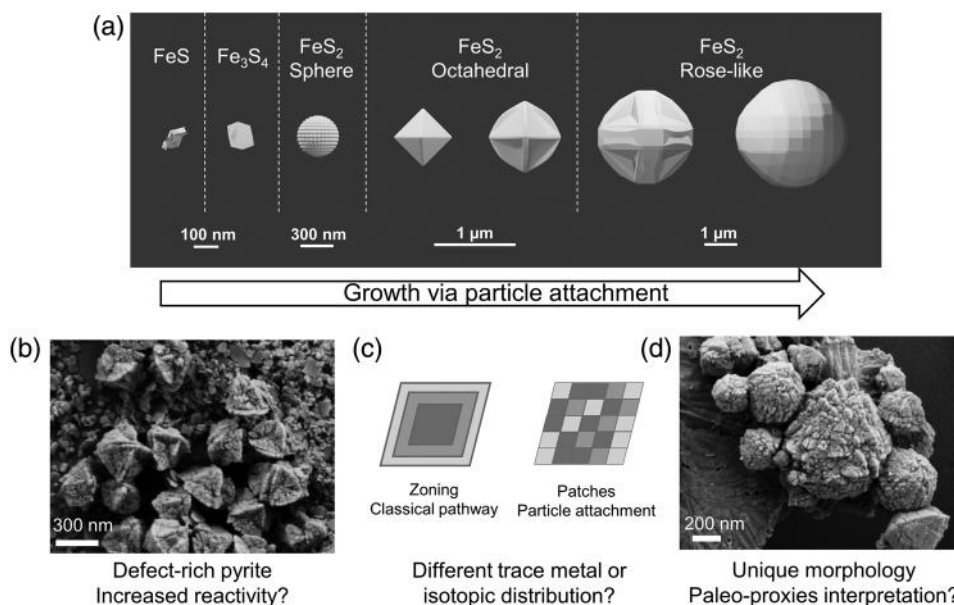

Figure 4 **(a)** Schematic of pyrite formation via particle attachment, showing skeletal growth and twinning between octahedral and rose-like particles (generated in Blender 3.2.2) and **(b–d)** the potential implications to the environment.

matter and biological activities, should be experimentally studied to determine their influence on pyrite morphologies and how these affect subsequent geological interpretations.

Particle Attachment Pathway

Detailed SEM analyses revealed two striking features: (1) particles existed in a continuum of size and shape, and (2) many of the larger particles had rough surface textures that indicate growth via aggregation of smaller particles with varying degrees of recrystallisation, similar in appearance to mesocrystals (Sturm and Cölfen, 2016). Similar surface features have been observed before and interpreted as screw dislocations (Wang and Morse, 1996; Butler and Rickard, 2000). We instead interpret these combined features imaged across multiple experiments as evidence for the particle attachment pathway (Fig. 2, 4) and propose the following transformation sequences. Initially, nanometer-scale FeS_{am} precipitated and transformed to tabular greigite particles (<150 nm). The tabular particles, perhaps in combination with nano-scale FeS_{am} particles, acted as primary units that attached together, forming larger aggregates (<100–250 nm). The aggregates tended to become less rounded and showed signs of recrystallisation towards particles with sharp edges, eventually forming octahedral particles (300–1500 nm). Pyrite containing multiple layers of flat particles and twinned developed into rose-like particles (1000–3000 nm). This morphology was the rarest type observed, and it was more common in *Set-2* compared to *Set-1* experiments. The developmental link between rose-like particles to other smaller particles was less clear. We propose that as particle attachment proceeded on octahedral pyrite, preferential stabilisation of the {111} faces are amplified, leading to a skeletal structure (Fig. 4), similar to those observed previously for ZnS (Xu *et al.*, 2016). The skeletal crystals continue to grow driven by higher attachment rates along the edges (Salas *et al.*, 2021) until they develop into a rose-like structure.

To our knowledge, this is the first time that pyrite formation via particle attachment has been described at <100 °C, leading to micro-framboid formation. *In situ* real-time microscopy observations will be crucial to confirm and describe the exact steps of this pathway. Studies aimed at investigating the subsequent effects on the reactivity and stability of pyrite grains, as well as the distribution of isotopes and trace metals, will help to constrain the potential implications to environmental proxies and biosignature interpretation (Fig. 4).

Acknowledgements

Additional Information

Supplementary Information accompanies this letter at https://www.geochemicalperspectivesletters.org/article2318.

Cite this letter as: Domingos, J.M., Runge, E., Dreher, C., Chiu, T.-H., Shuster, J., Fischer, S., Kappler, A., Duda, J.-P., Xu, J., Mansor, M. (2023) Inferred pyrite growth via the particle attachment pathway in the presence of trace metals. *Geochem. Persp. Let.* 26, 14–19. https://doi.org/10.7185/geochemlet.2318

References

ALLMAN, C.J., GÓMEZ-ORTIZ, D., BURKE, A., AMILS, R., RODRIGUEZ, N., FERNÁNDEZ-REMOLAR, D. (2021) Hydrogeochemical variability of the acidic springs in the Rio Tinto headwaters. *Water* 13, 2861. https://doi.org/10.3390/w13202861

BAYA, C., LE PAPE, P., BAPTISTE, B., MENGUY, N., DELBES, L., MORAND, M., ROUELLE, M., AUBRY, E., ONA-NGUEMA, G., NOËL, V. and JUILLOT, F. (2022) A methodological framework to study the behavior and kinetic influence of V, Mn, Co, Ni, Cu, Zn, As, Se and Mo during pyrite formation via the polysulfide pathway at ambient temperature. *Chemical Geology* 613. https://doi.org/10.1016/j.chemgeo.2022.121139

BUTLER, I.B., RICKARD, D. (2000) Framboidal pyrite formation via the oxidation of iron (II) monosulfide by hydrogen sulphide. *Geochimica et Cosmochimica Acta* 64, 2665–2672. https://doi.org/10.1016/S0016-7037(00)00387-2

CSÁKBERÉNYI-MALASICS, D., RODRIGUEZ-BLANCO, J.D., KIS, V.K., REČNIK, A., BENNING, L.G., PÓSFAI, M. (2012) Structural properties and transformations of precipitated FeS. *Chemical Geology* 294–295, 249–258. https://doi.org/10.1016/j.chemgeo.2011.12.009

DE YOREO, J.J., GILBERT, P.U., SOMMERDIJK, N.A., PENN, R.L., WHITELAM, S., JOESTER, D., ZHANG, H., RIMER, J.D., NAVROTSKY, A., BANFIELD, J.F. and WALLACE, A.F. (2015) Crystallization by particle attachment in synthetic, biogenic, and geologic environments. *Science* 349, aaa6760. https://doi.org/10.1126/science.aaa6760

ERICKSON, B.E., HELZ, G.R. (2000) Molybdenum(VI) speciation in sulfidic waters: Stability and lability of thiomolybdates. *Geochimica et Cosmochimica Acta* 64, 1149–1158. https://doi.org/10.1016/S0016-7037(99)00423-8

GONG, M., KIRKEMINDE, A., REN, S. (2013) Symmetry-defying iron pyrite (FeS₂) nanocrystals through oriented attachment. *Scientific Reports* 3, 1–6. https://doi.org/10.1038/srep02092

HUANG, F., GAO, W., GAO, S., MENG, L., ZHANG, Z., YAN, Y., REN, Y., LI, Y., LIU, K., XING, M. and WANG, Y. (2017) Morphology evolution of nano-micron pyrite: A review. *Journal of Nanoscience and Nanotechnology* 17, 5980–5995. https://doi.org/10.1166/jnn.2017.14430

HUNGER, S., BENNING, L.G. (2007) Greigite: A true intermediate on the polysulfide pathway to pyrite. *Geochemical Transactions* 8, 1–20. https://doi.org/10.1186/1467-4866-8-1

LI, W., DÖBLINGER, M., VANESKI, A., ROGACH, A.L., JÄCKEL, F., FELDMANN, J. (2011) Pyrite nanocrystals: Shape-controlled synthesis and tunable optical properties via reversible self-assembly. *Journal of Materials Chemistry* 21, 17946–17952. https://doi.org/10.1039/c1jm13336e

LIN, Z., SUN, X., PECKMANN, J., LU, Y., XU, L., STRAUSS, H., ZHOU, H., GONG, J., LU, H. and TEICHERT, B.M. (2016) How sulfate-driven anaerobic oxidation of methane affects the sulfur isotopic composition of pyrite: A SIMS study from the South China Sea. *Chemical Geology* 440, 26–41. https://doi.org/10.1016/j.chemgeo.2016.07.007

LIN, Z., SUN, X., LU, Y., STRAUSS, H., XU, L., GONG, J., TEICHERT, B.M., LU, R., LU, H., SUN, W. and PECKMANN, J. (2017) The enrichment of heavy iron isotopes in authigenic pyrite as a possible indicator of sulfate-driven anaerobic oxidation of methane: Insights from the South China Sea. *Chemical Geology* 449, 15–29. https://doi.org/10.1016/j.chemgeo.2016.11.032

LIU, K., HUANG, F., GAO, S., ZHANG, Z., REN, Y., AN, B. (2022) Morphology of framboidal pyrite and its textural evolution: Evidence from the Logatchev area, Mid-Atlantic Ridge. *Ore Geology Reviews* 141. https://doi.org/10.1016/j.oregeorev.2021.104630

LIU, W., LUO, C., ZHANG, S., ZHANG, B., MA, J., WANG, X., LIU, W., LI, Z., YANG, Q.H. and LV, W. (2021) Cobalt-doping of molybdenum disulfide for enhanced catalytic polysulfide conversion in lithium-sulfur batteries. *ACS Nano* 15, 7491–7499. https://doi.org/10.1021/acsnano.1c00896

MANSOR, M., FANTLE, M.S. (2019) A novel framework for interpreting pyrite-based Fe isotope records of the past. *Geochimica et Cosmochimica Acta* 253, 39–62. https://doi.org/10.1016/j.gca.2019.03.017

Mansor, M., Berti, D., Hochella Jr, M.F., Murayama, M., Xu, J. (2019) Phase, morphology, elemental composition and formation mechanisms of biogenic and abiogenic Fe-Cu-sulfide nanoparticles: A comparative study on their occurrences under anoxic conditions. *American Mineralogist* 104, 703–717. https://doi.org/10.2138/am-2019-6848

Miller, N., Dougherty, M., Du, R., Sauers, T., Yan, C., Pines, J.E., Meyers, K.L., Dang, Y.M., Nagle, E., Ni, Z. and Pungsrisai, T. (2020) Adsorption of tetrathiomolybdate to iron sulfides and its impact on iron sulfide transformations. *ACS Earth and Space Chemistry* 4, 2246–2260. https://doi.org/10.1021/acsearthspacechem.0c00176

Ohfuji, H., Rickard, D. (2005) Experimental syntheses of framboids - A review. *Earth-Science Reviews* 71, 147–170. https://doi.org/10.1016/j.earscirev.2005.02.001

Raiswell, R. (1982) Pyrite texture, isotopic composition and the availability of iron. *American Journal of Science* 282, 1244–1263. https://doi.org/10.2475/ajs.282.8.1244

Rickard, D. (2019) Sedimentary pyrite framboid size-frequency distributions: A meta-analysis. *Palaeogeography, Palaeoclimatology, Palaeoecology* 522, 62–75. https://doi.org/10.1016/j.palaeo.2019.03.010

Rickard, D., Luther, G.W. (2006) Metal sulfide complexes and clusters. *Reviews in Mineralogy and Geochemistry* 61, 421–504. https://doi.org/10.2138/rmg.2006.61.8

Robbins, L.J., Lalonde, S.V., Planavsky, N.J., Partin, C.A., Reinhard, C.T., Kendall, B., Scott, C., Hardisty, D.S., Gill, B.C., Alessi, D.S. and Dupont, C.L. (2016) Trace elements at the intersection of marine biological and geochemical evolution. *Earth-Science Reviews* 163, 323–348. https://doi.org/10.1016/j.earscirev.2016.10.013

Salas, P., Ruprecht, P., Hernández, L., Rabbia, O. (2021) Out-of-sequence skeletal growth causing oscillatory zoning in arc olivines. *Nature Communications* 12. https://doi.org/10.1038/s41467-021-24275-6

Sanden, S.A., Szilagyi, R.K., Li, Y., Kitadai, N., Webb, S.M., Yano, T., Nakamura, R., Hara, M., McGlynn, S.E. (2021) Electrochemically induced metal- vs. ligand-based redox changes in mackinawite: identification of a Fe^{3+}- and polysulfide-containing intermediate. *Dalton Transactions* 50, 11763–11774. https://doi.org/10.1039/D1DT01684A

Sawlowicz, Z. (1993) Pyrite framboids and their development: a new conceptual mechanism. *Geologische Rundschau* 82, 148–156. https://doi.org/10.1007/BF00563277

Shaw, T.J., Gieskes, J.M., Jahnke, R.A. (1990) Early diagenesis in differing depositional environments: The response of transition metals in pore water. *Geochimica et Cosmochimica Acta* 54, 1233–1246. https://doi.org/10.1016/0016-7037(90)90149-F

Sturm, E. V., Cölfen, H. (2016) Mesocrystals: Structural and morphogenetic aspects. *Chemical Society Reviews* 45, 5821–5833. https://doi.org/10.1039/C6CS00208K

Swanner, E.D., Webb, S.M., Kappler, A. (2019) Fate of cobalt and nickel in mackinawite during diagenetic pyrite formation. *American Mineralogist* 104, 917–928. https://doi.org/10.2138/am-2019-6834

Voelz, J.L., Johnson, N.W., Chun, C.L., Arnold, W.A., Penn, R.L. (2019) Quantitative dissolution of environmentally accessible iron residing in iron-rich minerals: A review. *ACS Earth and Space Chemistry* 3, 1371–1392. https://doi.org/10.1021/acsearthspacechem.9b00012

Von Damm, K.L., Edmond, J.M., Grant, B., Measures, C.I., Walden, B., Weiss, R.F. (1985) Chemistry of submarine hydrothermal solutions at 21°N, East Pacific Rise. *Geochimica et Cosmochimica Acta* 49, 2197–2220. https://doi.org/10.1016/0016-7037(85)90222-4

Wang, Q., Morse, J.W. (1996) Pyrite formation under conditions approximating those in anoxic sediments I. Pathway and morphology. *Marine Chemistry* 52, 99–121. https://doi.org/10.1016/0304-4203(95)00082-8

Wilkin, R.T., Barnes, H.L., Brantley, S.L. (1996) The size distribution of framboidal pyrite in modern sediments: An indicator of redox conditions. *Geochimica et Cosmochimica Acta* 60, 3897–3912. https://doi.org/10.1016/0016-7037(96)00209-8

Xu, J., Murayama, M., Roco, C.M., Veeramani, H., Michel, F.M., Rimstidt, J.D., Winkler, C., Hochella, M.F. (2016) Highly-defective nanocrystals of ZnS formed via dissimilatory bacterial sulfate reduction: A comparative study with their abiogenic analogues. *Geochimica et Cosmochimica Acta* 180, 1–14. https://doi.org/10.1016/j.gca.2016.02.007

Inferred pyrite growth via the particle attachment pathway in the presence of trace metals

J.M. Domingos, E. Runge, C. Dreher, T.-H. Chiu, J. Shuster, S. Fischer, A. Kappler, J.-P. Duda, J. Xu, M. Mansor

Supplementary Information

The Supplementary Information includes:

- ➢ Materials and Methods
- ➢ SI Discussion
- ➢ Tables S-1 to S-4
- ➢ Figure S-1 to S-3
- ➢ Supplementary Information References

Materials and Methods

Pyrite synthesis

Pyrite was synthesised using a modified method detailed in Mansor and Fantle (2019). Two sets of experiments were performed – one at the University of Texas at El Paso in 2019, and another at the University of Tuebingen in 2022. Differences between the two experimental sets are detailed in **Table S-2**. For both experimental sets, the following reagents were prepared in an anoxic glovebox: (1) 3 mM iron (Fe^{2+}) solution in 20 mM NaCl, (2) 180 mM sulphide solution, freshly prepared by dissolving $Na_2S \cdot 9H_2O$ in anoxic MQ H_2O on the same day of the experiment, (3) 1 M HEPES buffer, pH pre-adjusted to 7 with NaOH and (4) trace metal solutions (Co/Cu/Mo/Ni/Zn) either at 2 mM or 2 μM. Different trace metal concentrations were used to achieve a final metal:Fe ratio of either $1:10^2$ (*high-metal* experiments) or $1:10^5$ (*low-metal* experiments). Mixing of the reagents was performed in the glovebox in 100 ml-volume serum bottles. First, 10 mg of elemental sulphur (S^0) was pre-weighed into each bottle. Then, 30 ml of Fe^{2+} solution was aliquoted into each bottle, followed by the addition of 0.5 ml trace metals where applicable. Afterwards, 1.5 ml of HEPES buffer and 1 ml Na_2S were added, followed immediately by sealing of the bottles with butyl rubber stoppers and aluminum crimps. The final mixture contained approximately 3 mM Fe, 6 mM Na_2S, 30 mM S^0 and either 30 μM (*high-metal*) or 30 nM trace metals (*low-metal* experiments). The bottles were incubated statically at 25-80 °C in a dark incubator for up to 14 days. We employed static incubation to better represent environmental conditions in which materials are not consistently well-mixed, such as those found in natural sediments. Final pH was measured to be pH 7 ($\pm$ 0.1) with a pH probe, indicating the effectiveness of the HEPES buffer.

Polysulphides experiment and analysis

A set of bottles (1 bottle/condition) was prepared to determine the effects of trace metals on polysulphide formation following the protocol above. The only difference was the use of Fe-free NaCl instead of Fe^{2+} solution, which enabled better visualisation of the polysulphide coloration. After incubation, the solutions were sub-sampled, centrifuged at 20,000 x g for 2 minutes, and 200 µL of the supernatants were pipetted into a 96-well plate. Absorption was determined via UV-VIS spectroscopy from 250-550 nm, using the same experimental solution without Fe, S and trace metals as a blank.

Mineralogical analyses

Set-1 experiments were completely harvested (i.e., sacrificial sampling) for X-ray diffraction (XRD) and scanning electron microscopy (SEM). Initial attempts to collect the precipitates quantitatively via centrifugation or 0.22 µm filtration were unsuccessful due to the colloidal nature of the precipitates. Hence, aggregation and settling of the precipitates were first induced by adding 3 mL of anoxic 5 M NaCl, followed by incubation at 4 °C overnight. The overlying solution was carefully removed by pipetting. The precipitates were pooled into 1.5 mL tubes by repeated centrifugation at 2,000 x g for 5 minutes. The pellets were then washed 3x with 100 % ethanol (preventing colloidal behaviour) before resuspension to 1 mL in anoxic H_2O. An aliquot of ~800 µL was dried as a thin film onto glass slides for XRD analysis. The XRD patterns were collected using a Rigaku Miniflex II equipped with a Cu Kα source from 10-60° 2θ angle with a step size of 0.05° and a scan speed of 0.5°/min, totalling a collection time of 1 h 45 min. The remaining samples were diluted to 10 mL in anoxic H_2O and stored in sealed serum bottles for ~2 years prior to SEM analyses.

Aliquots of *Set-2* experiments were sub-sampled (repetitive sampling) for micro-XRD and SEM. For micro-XRD, around 5 mL was sampled, aggregation and settling induced by the addition of 5 M NaCl (1:10 NaCl:sample ratio) as before, washed 3x in ethanol and finally dried in the glovebox. Micro-XRD patterns of the dried pellets were collected on a Bruker's D8 Discover GADDS XRD2 equipped with a Co Kα source from 5.6-69.1° 2θ angle with a step size of 0.05° and a scan speed of 0.265°/sec, totalling 4 minutes of scanning time (Berthold *et al.*, 2009). For all XRD analyses throughout this study, samples were transferred from the glovebox to the instrument within air-tight containers. Exposure to air was unavoidable during analysis. However, oxidation and transformation of dried Fe sulphides is not expected within the scanning times employed in this study (Boursiquot *et al.*, 2001).

For SEM analysis of both experimental sets, aliquots (50 uL) of the samples were placed directly onto carbon adhesive tabs attached to aluminium stubs. Excess solution was allowed to air-dry overnight within an anaerobic chamber. Once dry, the samples were removed from the glovebox, immediately coated with an 8 nm-thick deposition of gold or platinum using a BAL-TEC™ SCD 005 sputter coater and imaged within the same day. The precipitates were characterised using a Zeiss Crossbeam 550L Scanning Electron Microscope (SEM) equipped with an Oxford Instrument Energy Dispersive Spectrometer (EDS). All micrographs were taken in Secondary Electron (SE) mode with an accelerating voltage of 2 kV. An additional subset of samples was dissolved in 6 M HCl for 10 minutes before SEM imaging to differentiate between HCl-soluble minerals (FeS_{am}, mackinawite, greigite) and HCl-insoluble mineral (pyrite).

The relative XRD signal intensities of pyrite/greigite – a proxy for the extent of pyrite formation – were determined by dividing the height of the main pyrite signal at 33° 2θ with the greigite signal at 30° 2θ (Cu Kα). This approach is only valid when mackinawite is absent, as it also contributes to the 30° signal. Furthermore, this approach does not consider crystallinity variation, which can cause signal broadenings that decrease peak heights. Analyses of duplicate bottles of *no-metals* and *low-metal* Co *Set 1* experiments indicated an error of 0.25 and 0.23, respectively. We conservatively assumed an error of ± 0.25 for all experiments.

SI Discussion

Calculation of pyrite formation rates and potential effects of H$_2$

For *Set-1* experiments, we used the Match! Software (https://www.crystalimpact.com/match/) to semi-quantitatively obtain the relative abundance of pyrite over greigite at day 14 in the presence of various trace metals. With pyrite's relative abundance of 55-78 % and initial Fe concentration of 3 mM, we calculated formation rates of 1.5-1.9 x 10^{-9} mol/L/s.

For *Set-2* experiments, pyritisation was complete within 3 days and earlier time points were not measured. We therefore calculated a minimum formation rate of 1.2 x 10^{-8} mol/L/s. Hence, *Set-2* experiments exhibited at least 10 times faster pyrite formation than *Set-1* experiments.

In our study, pyrite forms via two parallel pathways:

H$_2$S pathway:

$$FeS_{aq} + H_2S \rightarrow FeS_2 + H_2 \tag{1}$$

Polysulphide pathway:

$$H_2S + S^0 \rightarrow S_2^{2-} + 2\,H^+ \tag{2}$$
$$FeS_{aq} + S_2^{2-} \rightarrow FeS_2 + S^{2-} \tag{3}$$

Pyritisation via the polysulphide pathway is more important in our study given the presence of S^0 and limited H$_2$S$_{(aq)}$ from the speciation of H$_2$S$_{(aq)}$/HS$^-$ at pH 7 (Mansor and Fantle, 2019). The range of the rate in this study of 10^{-9} to 10^{-8} mol/L/s is similar to those of the 80 °C experiments of Mansor and Fantle (2019) and room temperature pyritisation via the ferric-hydroxide-surface (FHS) pathway (Wan *et al.*, 2017). It is however slightly faster than average rates determined from marine sediments (compiled in Mansor and Fantle, 2019). The relative importance of different pyrite formation pathways in various environments is an open question. Peiffer *et al.*, (2015) noted that the FHS pathway operates at high Fe(III)/S(-II) ratio such as in freshwater systems or at various sediment-water interfaces where sulphide concentration is low, while the polysulphide/H$_2$S pathways tend to operate deeper in the subsurface in environments rich with sulphate and organic matter that promote microbial sulphate reduction. A recent study noted that the FHS pathway could still operate in deeper sediments under high burial rates (Liu *et al.*, 2021). Hence, the mode of pyrite growth in our study could be applicable to nature given the similarities in the observed rates.

To explore how H_2 can affect pyrite formation via the polysulphide pathway in experimental setups, we first calculated the aqueous concentration of H_2 at equilibrium with 3 % H_2 (1 bar) in the glovebox based on Henry's Law (Sander, 2015) to be 23 μM. We then calculated the Eh of different redox couples in Phreeqc using Minteq database version 4 under the specified experimental condition (pH 7, 3 mM Fe^{2+}, 6 mM Na_2S, 20 mM NaCl, varying $H_{2(aq)}$). The S(-2)/S(6) redox couple has an Eh of -209 mV. The Eh of the H(0)/H(1) redox couple decreases from -203 to -361 mV from negligible concentration to 23 μM $H_{2(aq)}$. Previous studies have noted that pyrite formation is faster under more oxidising conditions (Benning *et al.*, 2000; Butler and Rickard, 2000; Rickard and Luther, 2007) and that different glovebox gas compositions affected whether FeS_{am} or crystalline mackinawite was formed (Csákberényi-Malasics *et al.*, 2012). Rickard and Luther (2007) noted that Eh variations between -200 to -361 mV could greatly affect polysulphide speciation and pyrite supersaturation state at near-neutral pH. Hence, even small quantities of H_2 have the potential to decrease Eh and to slow down pyrite formation.

Disparities in how trace metals affected pyrite formation kinetics

In our *Set-1* experiments, XRD analyses suggested that all tested trace metals (Mo, Ni, Cu, Zn, Co) accelerated pyrite formation relative to when no trace metals were added (**Fig. 1b**). These observations are consistent with many studies (**Table S-1**). However, several disparities exist.

First, Swanner *et al.*, (2019) showed that Co and Ni inhibited pyrite formation at relatively high trace metal to Fe ratios (0.002-0.007 versus 10^{-5} in this study). They synthesised pyrite by reacting 33 mM of dried mackinawite (co-precipitated with Ni or Co to a final concentration of ~0.16 mM in the mixture) with 50 mg of S^0 in pH 6 phthalate buffer for 2 weeks at 65 °C. The final solution volume was not specified – therefore, the total S/Fe ratio is unclear. It was suggested that Co and Ni incorporation into mackinawite increased the mineral's crystallinity, making it less susceptible to dissolution-reprecipitation reactions towards pyrite formation (Baya *et al.*, 2021; Ikogou *et al.*, 2017). Given that we utilised much lower trace metal to Fe ratios, it is likely that the FeS_{am} formed in our experiments were not so affected by this increase in crystallinity. Other studies that tested Ni observed similar accelerating effects as in our study (Morin *et al.*, 2017; Baya *et al.*, 2021; 2022), attributed to the formation of Ni-rich nanoparticles that acted as nuclei for pyrite formation. Those studies did employ similar trace metal to Fe ratios as Swanner *et al.* (2019), but pyrite synthesis was achieved at a pH of 5.5, wherein NiS is one orders of magnitude less soluble than at pH 6 (Mansor *et al.*, 2019). Hence, the formation of NiS that can act as nuclei for pyrite formation becomes more likely under the acidic condition employed in those studies.

The mechanism of how Co can accelerate pyrite formation is less clear than for Ni. Our study is the first to show that Co actually facilitates more polysulphide formation compared to other trace metals tested (**Fig. 3**). A previous study showed that Co substitutes easily into FeS and that the crystallinity of Co-substituted FeS decreases with higher Co content (Mansor *et al.*, 2020), in contrast to what Swanner *et al.*, (2019) observed. We hypothesize that in our current study, the low Co content did not greatly affect the crystallinity of FeS_{am} while it simultaneously facilitated polysulphide formation.

Next, Baya et $al.$, (2022) showed that Mo inhibited pyrite formation at trace metal to Fe ratios of 0.005, which is higher than the ratio of 10^{-5} in this study. They synthesised pyrite by reacting 75 mM aqueous $FeCl_3$ with 75 mM Na_2S at pH 5.5 for up to 129 days at room temperature. They proposed that the formation of colloidal Fe-Mo-S clusters inhibits pyrite formation by slowing down the interaction between polysulphides and Mo-free FeS_x clusters. We hypothesize that the difference in synthesis pH affects the formation of colloidal Fe-Mo-S clusters (Vorlicek et $al.$, 2018) and subsequently how Mo influence pyrite formation. At our experimental pH of 7 and relatively low Mo concentration, less colloidal Fe-Mo-S clusters are expected. Hence, Mo(VI) could function as an oxidant to accelerate pyrite formation at near-neutral pH, consistent with other studies (Mansor and Fantle, 2019; Miller et $al.$, 2020).

Supplementary Tables
Table S-1 Summary of experiments that studied the influence of trace metals on pyrite formation.

Metal	Initial metal/Fe molar ratio	Influence on precipitation rate	Influence on morphology	Synthesis conditions	Proposed mechanism(s)	Reference
As (III)	0.001	Inhibit	?	50 mM $FeCl_3$ + 50 mM Na_2S at pH 5.2-5.8 for 9 weeks at room temperature	Sorption to FeS/pyrite, passivation by As_2S_3, interference of polysulphide formation by forming As-(poly)sulphide complexes	(Baya *et al.*, 2021)
As (III)	10^{-7} to 10	Inhibit	?	9 mM freeze-dried FeS + 18 mM H_2S + Ti(III) citrate in pH 6 phosphate buffer		(Wolthers *et al.*, 2007)
As (III)	0.005	Inhibit	?*	75 mM $FeCl_3$ + 75 mM Na_2S at pH 5.5 for 129 days at room temperature		(Baya *et al.*, 2022)
As(V)	10^{-5} to 10	Inhibit	?	9 mM freeze-dried FeS + 18 mM H_2S + Ti(III) citrate in pH 6 phosphate buffer		(Wolthers *et al.*, 2007)
Co	0.007	Inhibit	?	33 mM dried mackinawite + 50 mg S^0 in pH 6 phthalate buffer for 2 weeks at 65°C. Final solution volume not specified.	Co incorporation increased mackinawite's crystallinity, making it less susceptible to dissolution-reprecipitation reactions (proposed by Baya *et al.*, 2021)	(Swanner *et al.*, 2019)
Co	0.005	Accelerate	?*	75 mM $FeCl_3$ + 75 mM Na_2S at pH 5.5 for 129 days at room temperature	-	(Baya *et al.*, 2022)
Co	0.11	No data	Same shape but smaller size	100 mM FeS + 100 mM polysulphides for 12 hours at 160°C	-	(Lin *et al.*, 2022)

Table S-1 continued Summary of experiments that studied the influence of trace metals on pyrite formation.

Metal	Initial metal/Fe molar ratio	Influence on precipitation rate	Influence on morphology	Synthesis conditions	Proposed mechanism(s)	Reference
Co	10^{-5}	Accelerate	No effect	3 mM Fe^{2+} + 6 mM Na_2S + 30 mM S^0 in pH 7 HEPES buffer for 2 weeks at 80°C	Facilitation of polysulphide formation / acceleration of nucleation	*This study*
Cu	10^{-5}	Accelerate	No effect	3 mM Fe^{2+} + 6 mM Na_2S + 30 mM S^0 in pH 7 HEPES buffer for 2 weeks at 80°C	Facilitation of polysulphide formation / acceleration of nucleation	*This study*
Cu	0.005	Accelerate	?*	75 mM $FeCl_3$ + 75 mM Na_2S at pH 5.5 for 129 days at room temperature	-	(Baya *et al.*, 2022)
Cu	0.1-3.5	Inhibit	-	1:3 Fe:S ratio sonicated for 15 min in diethanolamine and ethanol, then heated for 18 h at 100°C	Enhanced crystallinity and stabilisation of mackinawite by Cu; formation of secondary Cu-Fe mixed phases	(Zavašnik *et al.*, 2014)
Mo	0.00003 to 0.03	Accelerate	?	3 mM Fe^{2+} + 6 mM Na_2S + 10 mM S^0 in pH 7 HEPES buffer for 1 week at 80°C	-	(Mansor and Fantle, 2019)
Mo	0.005 to 0.05	Accelerate	?	60 mg mackinawite/greigite mixture (~135 mM Fe) heated in H_2O for 9 minutes from 80-200°C	Mo(VI) stabilises greigite and accelerates pyrite formation by acting as an oxidant, becoming reduced to Mo(IV) in the process.	(Miller *et al.*, 2020)
Mo	10^{-5}	Accelerate	No effect	3 mM Fe^{2+} + 6 mM Na_2S + 30 mM S^0 in pH 7 HEPES buffer for 2 weeks at 80°C		*This study*
Mo	0.005	Inhibit	?*	75 mM $FeCl_3$ + 75 mM Na_2S at pH 5.5 for 129 days at room temperature	Formation of colloidal Fe-Mo-S clusters slows down interaction of polysulphides with FeS_x clusters	(Baya *et al.*, 2022)

Table S-1 continued Summary of experiments that studied the influence of trace metals on pyrite formation.

Metal	Initial metal/Fe molar ratio	Influence on precipitation rate	Influence on morphology	Synthesis conditions	Proposed mechanism(s)	Reference
Mn	0.005	Accelerate	?*	75 mM $FeCl_3$ + 75 mM Na_2S at pH 5.5 for 129 days at room temperature	-	(Baya et al., 2022)
Mn	0.11	No data	No effect	100 mM FeS + 100 mM polysulphides for 12 hours at 160 °C	-	(Lin et al., 2022)
Ni	10^{-5}	Accelerate	No effect	3 mM Fe^{2+} + 6 mM Na_2S + 30 mM S^0 in pH 7 HEPES buffer for 2 weeks at 80 °C	Facilitation of polysulphide formation / acceleration of nucleation	*This study*
Ni	0.001	Accelerate	?	50 mM $FeCl_3$ + 50 mM Na_2S at pH 5.2-5.8 for 9 weeks at room temperature	Ni accelerated pyrite nucleation	(Baya et al., 2021)
Ni	0.01	Accelerate	?	50 mM $FeCl_3$ + 50 mM Na_2S at pH 5.2-5.8 for 2 weeks at room temperature	Ni accelerated pyrite nucleation	(Morin et al., 2017)
Ni	0.005	Accelerate	?*	75 mM $FeCl_3$ + 75 mM Na_2S at pH 5.5 for 129 days at room temperature	Ni accelerated pyrite nucleation	(Baya et al., 2022)
Ni	0.11	No data	Smaller size and shape change from cubic to octahedral	100 mM FeS + 100 mM polysulphides for 12 hours at 160 °C	-	(Lin et al., 2022)
Ni	0.002	Inhibit	?	33 mM dried mackinawite + 50 mg S^0 in pH 6 phthalate buffer for 2 weeks at 65 °C. Final solution volume not specified.	Ni incorporation increased mackinawite's crystallinity, making it less susceptible to dissolution-reprecipitation reactions (proposed by Baya et al., 2021)	(Swanner et al., 2019)

Table S-1 continued Summary of experiments that studied the influence of trace metals on pyrite formation.

Metal	Initial metal/Fe molar ratio	Influence on precipitation rate	Influence on morphology	Synthesis conditions	Proposed mechanism(s)	Reference
Se	0.005	Accelerate	?*	75 mM $FeCl_3$ + 75 mM Na_2S at pH 5.5 for 129 days at room temperature	-	(Baya *et al.*, 2022)
V	0.005	Inhibit	?*	75 mM $FeCl_3$ + 75 mM Na_2S at pH 5.5 for 129 days at room temperature	-	(Baya *et al.*, 2022)
Zn	10^{-5}	Accelerate	No effect	3 mM Fe^{2+} + 6 mM Na_2S + 30 mM S^0 in pH 7 HEPES buffer for 2 weeks at 80 °C	Facilitation of polysulphide formation / acceleration of nucleation	*This study*
Zn	0.005	Accelerate	?*	75 mM $FeCl_3$ + 75 mM Na_2S at pH 5.5 for 129 days at room temperature	-	(Baya *et al.*, 2022)

*Electron microscopy images showed increasing sizes in the < 1 μm size range in the order of As < Mo < Ni < Co < Zn < Se, but corresponding data on trace metal-free pyrite are not available

Table S-2 Differences between *Set-1* and *Set-2* experiments.

	Set-1	*Set-2*
Location **Year**	University of Texas at El Paso 2019	University of Tuebingen 2022
Experimental design	Sacrificial sampling. *No-metals* and *low-metals* experiments from 25-80 °C	Repetitive sampling. *No-metals, low-metal* Co, *high-metals* and Polysulphide experiments at 80 °C
Glovebox and headspace	CoyLab, 97% N_2 - 3% H_2	MBraun, 100% N_2
XRD	Thin film on glass slides, Rigaku Miniflex II, Cu Kα source, 1 h 45 min collection time	Dried pellets, Bruker's D8 Discover GADDS XRD2, Co Kα source, 240 seconds collection time
Storage details before SEM	~2 years in anoxic water at ambient temperature	< 2 weeks in anoxic water at ambient temperature
Reagents	$(NH_4)_2Fe(SO_4)_2 \cdot 6H_2O$ $Na_2S.9H_2O$ S^0; Alfa Aesar product #10785 $CoCl_2 \cdot 6H_2O$ $CuCl_2 \cdot 2H_2O$ $Na_2MoO_4 \cdot 2H_2O$ $NiCl_2 \cdot 6H_2O$ $ZnCl_2$	$FeSO_4.7H_2O$ $Na_2S.9H_2O$ S^0; Sigma Aldrich product #13803 $Co(NO_3)_2 \cdot 6H_2O$ $CuCl_2 \cdot 2H_2O$ $Na_2MoO_4 \cdot 2H_2O$ $NiCl_2 \cdot 6H_2O$ $ZnCl_2$

Table S-3 Summary of experimental conditions, the type of analyses (SEM, magnetism) and the mineralogy as determined by XRD.

Exp	Temp (°C)	Time (days)	Condition	SEM	XRD detection					Magnetism
					FeS_{am}	Greigite	Pyrite	S^0	NaCl	
Set 1	25	7	NoMetal		+			+		NM
	40	7	NoMetal		+			+	+	NM
	40	14	NoMetal	✓	+	+		+	+	NM
	60	7	NoMetal		+	+		+	+	NM
			LowCo		+	+		+		NM
			LowCu		+	+		+		NM
			LowNi		+	+			+	NM
			LowZn		+	+		+	+	NM
	60	14	NoMetal		+	+	+	+	+	NM
			LowCo		+	+	+	+	+	NM
			LowCu		+	+	+		+	NM
			LowNi		+	+	+	+	+	NM
			LowZn		+	+	+		+	NM
	80	14	NoMetal 1	✓		+	+	+		NM
			NoMetal 2			+	+	+		NM
			LowCo 1	✓		+	+	+		NM
			LowCo 2			+	+	+		NM
			LowCu	✓		+	+	+		NM
			LowMo	✓		+	+	+		NM
			LowNi	✓		+	+	+		NM
			LowZn	✓		+	+	+		NM
Set 2	80	0	LowCo	✓	+					-
		3		✓			+			Light
		7		✓			+			Light
		14		✓			+			Light
	80	7	NoMetal		Insufficient sample					Light
			HighCo				+			Light
			HighCu				+			Light
			HighMo		Insufficient sample					Strong
			HighNi		Insufficient sample					Light
			HighZn				+	+		Light
		14	NoMetal	✓			+	+		Light
			HighCo	✓			+	+		Light
			HighCu	✓			+			Light
			HighMo	✓			+	+		Medium
			HighNi	✓			+	+		Light
			HighZn	✓			+			Light

*S^0 and NaCl are residues from the starting materials.

#Magnetic minerals probed with a hand magnet. NM = not measured.

Table S-4 Metadata for SEM images shown in the main text Fig. 2 and Fig. 4

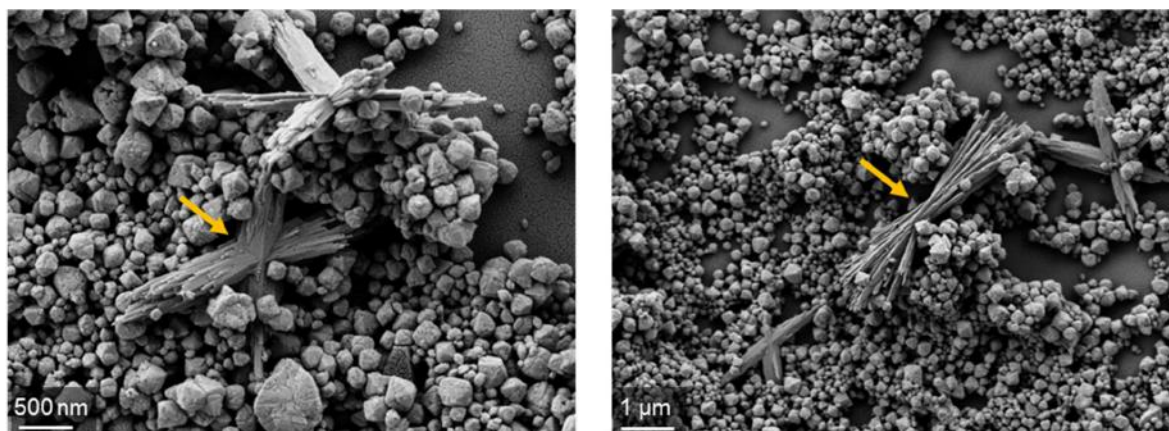| Figure	Exp	Temp (°C)	Time (days)	Condition
2a	*Set 2*	80	0	LowCo
2b	*Set 1*	40	14	NoMe
2c	*Set 1*	40	14	NoMe
2d	*Set 1*	80	14	NoMe
2e	*Set 2*	80	7	HighZn
2f	*Set 1*	80	14	NoMe
2g	*Set 1*	40	14	NoMe
4b	*Set 1*	40	14	NoMe
4d	*Set 2*	80	7	HighZn

Supplementary Figures

Figure S-1 Representative SEM images of Fe- and oxygen-rich acicular minerals (yellow arrows) in samples from the *Set-2* experiments. The acicular minerals are surrounded by pyrite octahedra of different sizes and degrees of sharp edges. The acicular minerals exhibit twinning features and are reminiscent of goethite (FeOOH), although the mineralogy still needs to be confirmed via techniques such as transmission electron microscopy. Fe(III) (oxyhydr)oxides were not detected with XRD, suggesting low relative abundances.
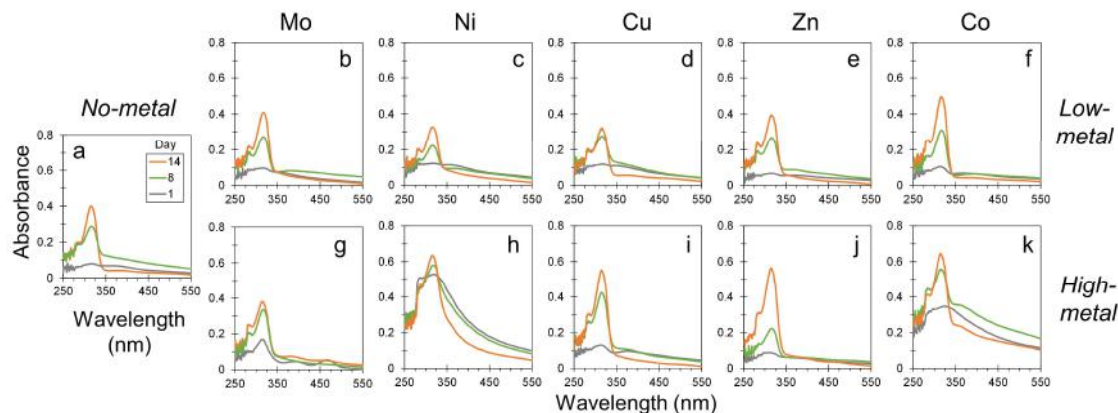
Figure S-2 Absorption spectra of polysulphides in the **(a)** *No-metal* (middle left)*,* **(b-f)** *low-metal* (top row) and **(g-k)** *high-metal* (bottom row) setups at day 1, 8 and 14. Note that (i) enhancements of formation of polysulphides are evident by peaks at 275 and 314 nm, (ii) higher trace metals generally lead to more polysulphide formation, except for Mo, (iii) different trace metals result in different ratios of the 275 and 314 nm peaks, most likely indicating different polysulphide distribution (S_nS^{2-}; different *n* values) and (iv) longer incubation time generally lead to more polysulphides, with the exception of the HighNi setup in which the polysulphide distribution has most likely evolved over time. Individual polysulphide species cannot be identified based on their spectrum alone (Steudel and Chivers, 2019; Kamyshny *et al.*, 2004).

Experiments

Set 1   Set 2
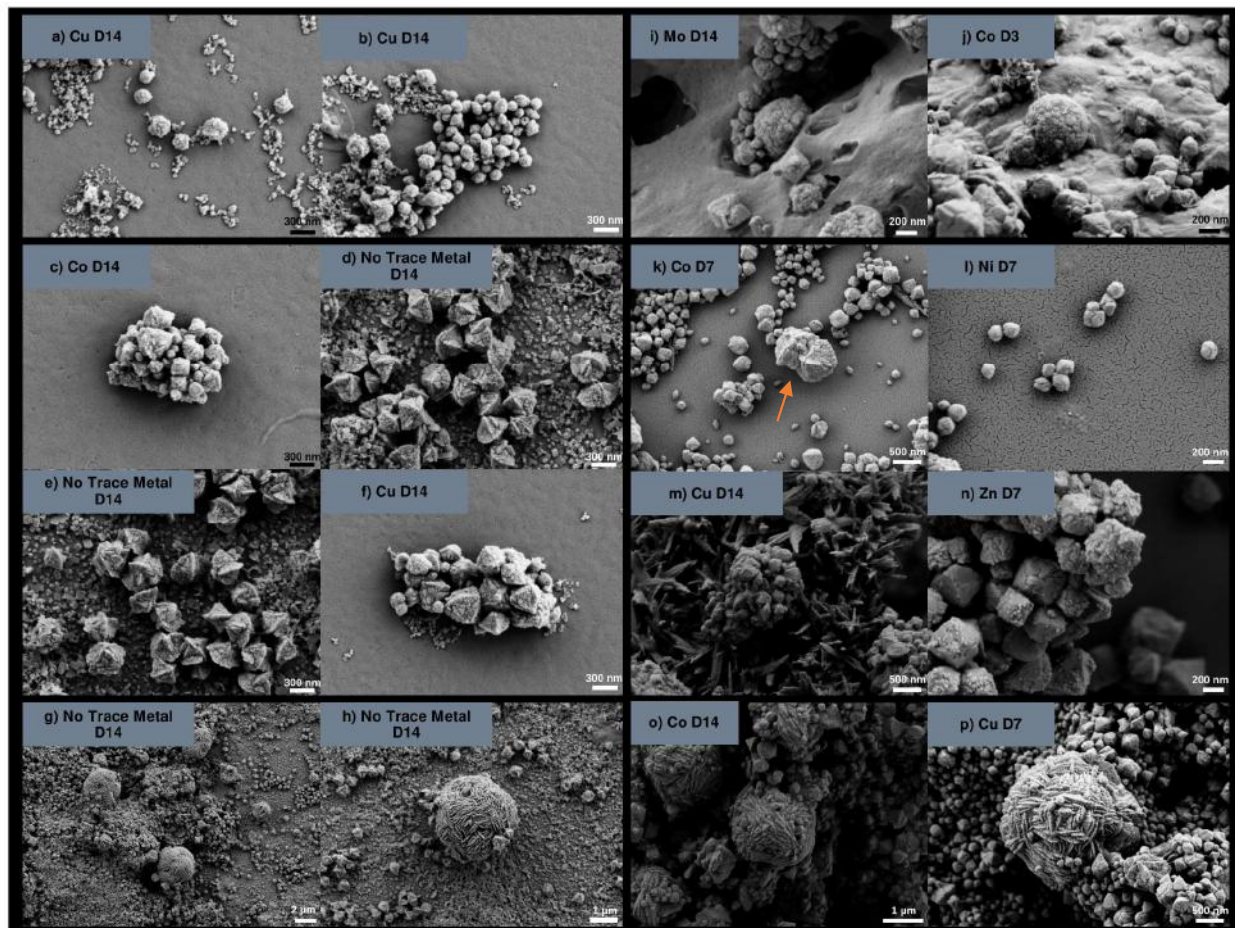

Figure S-3 Comparison of particle morphologies across experiments with varying trace metals. **(a)** Spherical aggregates surrounded by smaller nanoparticles; **(b)** spherical aggregates of varying sizes that are morphing into sharp-edged euhedral crystals; **(c)** agglomerated spherical & octahedral crystals; **(d)** octahedral crystals with extended edges surrounded by smaller tabular nanoparticles; **(e)** octahedral crystals with extended edges surrounded by smaller tabular nanoparticles; **(f)** agglomerated octahedral crystals; **(g)** rose-like crystals surrounded by octahedral crystals and smaller nanoparticles; **(h)** a rose-like crystal surrounded by octahedral crystals and smaller nanoparticles; **(i)** spherical aggregates with octahedral crystals; **(j)** multiple spherical aggregates surrounded by some octahedral crystals; **(k)** a penetration twin (orange arrow) of two octahedral crystals with extended edges surrounded by smaller octahedral crystals; **(l)** spherical aggregates morphing into octahedral crystals; **(m)** agglomerated octahedral crystals; **(n)** multiple octahedral crystals with porous surfaces; **(o)** multiple rose-like

crystals with octahedral crystals in-between; **(p)** rose-like crystal surrounded by octahedral crystals. Note that surface roughness of pyrite has been observed experimentally before but they were not directly linked to growth via particle attachment.

Supplementary Information References

Baya, C., Le Pape, P., Baptiste, B., Brest, J., Landrot, G., Elkaim, E., Noël, V., Blanchard, M., Ona-Nguema, G., Juillot, F. and Morin, G. (2021) Influence of trace level As or Ni on pyrite formation kinetics at low temperature. *Geochimica et Cosmochimica Acta* 300, 333–353. https://doi.org/10.1016/j.gca.2021.01.042

Baya, C., Le Pape, P., Baptiste, B., Menguy, N., Delbes, L., Morand, M., Rouelle, M., Aubry, E., Ona-Nguema, G., Noël, V. and Juillot, F., (2022) A methodological framework to study the behavior and kinetic influence of V, Mn, Co, Ni, Cu, Zn, As, Se and Mo during pyrite formation via the polysulfide pathway at ambient temperature. *Chemical Geology* 613. https://doi.org/10.1016/j.chemgeo.2022.121139

Benning, L.G., Wilkin, R.T., Barnes, H.L. (2000) Reaction pathways in the Fe-S system below 100^0C. *Chemical Geology* 167, 25–51. https://doi.org/10.1016/S0009-2541(99)00198-9

Berthold, C., Bjeoumikhov, A., Brügemann, L. (2009) Fast XRD^2 microdiffraction with focusing X-Ray microlenses. *Particle and Particle Systems Characterization* 26, 107–111. https://doi.org/10.1002/ppsc.200800038

Boursiquot, S., Mullet, M., Abdelmoula, M., Génin, J.-M., Ehrhardt, J.-J. (2001) The dry oxidation of tetragonal FeS_{1-x} mackinawite. *Physics and Chemistry of Minerals* 28, 600–611. https://doi.org/10.1007/s002690100193

Butler, I.B., Rickard, D. (2000) Framboidal pyrite formation via the oxidation of iron (II) monosulfide by hydrogen sulphide. *Geochimica et Cosmochimica Acta* 64, 2665–2672. https://doi.org/10.1016/S0016-7037(00)00387-2

Csákberényi-Malasics, D., Rodriguez-Blanco, J.D., Kis, V.K., Rečnik, A., Benning, L.G., Pósfai, M. (2012) Structural properties and transformations of precipitated FeS. *Chemical Geology* 294–295, 249–258. https://doi.org/10.1016/j.chemgeo.2011.12.009

Ikogou, M., Ona-Nguema, G., Juillot, F., Le Pape, P., Menguy, N., Richeux, N., Guigner, J.M., Noël, V., Brest, J., Baptiste, B. and Morin, G. (2017) Long-term sequestration of nickel in mackinawite formed by *Desulfovibrio capillatus* upon Fe(III)-citrate reduction in the presence of thiosulfate. *Applied Geochemistry* 80, 143–154. https://doi.org/10.1016/j.apgeochem.2017.02.019

Kamyshny, A., Goifman, A., Gun, J., Rizkov, D., Lev, O. (2004) Equilibrium distribution of polysulfide ions in aqueous solutions at 25 degrees C: a new approach for the study of polysulfides' equilibria. *Environmental science & technology* 38, 6633–6644. https://doi.org/10.1021/es049514e

Lin, X., Xia, Y., Wei, G., Zhou, J., Liang, X., Xian, H., Zhu, J., He, H. (2022) Distinct effects of transition metal (cobalt, manganese and nickel) ion substitutions on the abiotic oxidation of pyrite: In view of hydroxyl radical production. *Geochimica et Cosmochimica Acta* 321, 170–183. https://doi.org/10.1016/j.gca.2022.01.026

Liu, J., Antler, G., Pellerin, A., Izon, G., Dohrmann, I., Findlay, A.J., Røy, H., Ono, S., Turchyn, A.V., Kasten, S. and Jørgensen, B.B., (2021) Isotopically "heavy" pyrite in marine sediments due to high sedimentation rates and non-steady-state deposition. *Geology* 49, 816–821. https://doi.org/10.1130/G48415.1

Mansor, M., Fantle, M.S. (2019) A novel framework for interpreting pyrite-based Fe isotope records of the past. *Geochimica et Cosmochimica Acta* 253, 39–62. https://doi.org/10.1016/j.gca.2019.03.017

Mansor, M., Winkler, C., Hochella Jr, M.F., Xu, J. (2019) Nanoparticulate nickel-hosting phases in sulfidic environments: Effects of ferrous iron and bacterial presence on mineral

formation mechanism and solid-phase nickel distribution. *Frontiers in Earth Science - Earth and Planetary Materials* 7, 151. https://doi.org/10.3389/feart.2019.00151

Mansor, M., Cantando, E., Wang, Y., Hernandez-Viezcas, J.A., Gardea-Torresdey, J.L., Hochella Jr., M.F., Xu, J. (2020) Insights into the biogeochemical cycling of cobalt: Precipitation and transformation of cobalt sulfide nanoparticles under low-temperature aqueous conditions. *Environmental Science and Technology* 54, 5598–5607. https://doi.org/10.1021/acs.est.0c01363

Miller, N., Dougherty, M., Du, R., Sauers, T., Yan, C., Pines, J.E., Meyers, K.L., Dang, Y.M., Nagle, E., Ni, Z. and Pungsrisai, T., (2020) Adsorption of tetrathiomolybdate to iron sulfides and its impact on iron sulfide transformations. *ACS Earth and Space Chemistry* 4, 2246–2260. https://doi.org/10.1021/acsearthspacechem.0c00176

Morin, G., Noël, V., Menguy, N., Brest, J., Baptiste, B., Tharaud, M., Ona-Nguema, G., Ikogou, M., Viollier, E. and Juillot, F. (2017) Nickel accelerates pyrite nucleation at ambient temperature. *Geochemical Perspectives Letters* 6–11. https://doi.org/10.7185/geochemlet.1738

Peiffer, S., Behrends, T., Hellige, K., Larese-Casanova, P., Wan, M., Pollok, K. (2015) Pyrite formation and mineral transformation pathways upon sulfidation of ferric hydroxides depend on mineral type and sulfide concentration. *Chemical Geology* 400, 44–55. https://doi.org/10.1016/j.chemgeo.2015.01.023

Rickard, D., Luther, G.W. (2007) Chemistry of iron sulfides. *Chemical Reviews* 107, 514–562. https://doi.org/10.1021/cr0503658

Sander, R. (2015) Compilation of Henry's law constants (version 4.0) for water as solvent. *Atmospheric Chemistry and Physics* 15, 4399–4981. https://doi.org/10.5194/acp-15-4399-2015

Steudel, R., Chivers, T. (2019) The role of polysulfide dianions and radical anions in the chemical, physical and biological sciences, including sulfur-based batteries. *Chemical Society Reviews* 48, 3279–3319. https://doi.org/10.1039/C8CS00826D

Swanner, E.D., Webb, S.M., Kappler, A. (2019) Fate of cobalt and nickel in mackinawite during diagenetic pyrite formation. *American Mineralogist* 104, 917–928. https://doi.org/10.2138/am-2019-6834

Vorlicek, T.P., Helz, G.R., Chappaz, A., Vue, P., Vezina, A., Hunter, W. (2018) Molybdenum burial mechanism in sulfidic sediments: Iron-sulfide pathway. *ACS Earth and Space Chemistry* 2, 565–576. https://doi.org/10.1021/acsearthspacechem.8b00016

Wan, M., Schröder, C., Peiffer, S. (2017) Fe(III):S(-II) concentration ratio controls the pathway and the kinetics of pyrite formation during sulfidation of ferric hydroxides. *Geochimica et Cosmochimica Acta* 217, 334–348. https://doi.org/10.1016/j.gca.2017.08.036

Wolthers, M., Butler, I.B., Rickard, D. (2007) Influence of arsenic on iron sulfide transformations. *Chemical Geology* 236, 217–227. https://doi.org/10.1016/j.chemgeo.2006.09.010

Zavašnik, J., Stanković, N., Arshad, S.M., Rečnik, A. (2014) Sonochemical synthesis of mackinawite and the role of Cu addition on phase transformations in the Fe-S system. *Journal of Nanoparticle Research* 16. https://doi.org/10.1007/s11051-013-2223-z